MTLA 38 (2024) 102234

Contents lists available at ScienceDirect

Materialia

journal homepage: www.elsevier.com/locate/mtla

Mechanical response of LPBFed TI64 thickness graded Voronoi lattice structures

Chiara Bregoli [a,c,*], Jacopo Fiocchi [a], Mehrshad Mehrpouya [b], Laura Maria Vergani [c], Ausonio Tuissi [a], Carlo Alberto Biffi [a]

[a] National Research Council, CNR-ICMTE, Lecco, Italy
[b] University of Twente, Faculty of Engineering Technology, Enschede, the Netherlands
[c] Politecnico di Milano, Mechanical Engineering Department, Milano, Italy

ARTICLE INFO

Keywords:
Functional graded structures
Voronoi tessellation
Energy absorption
Laser powder bed fusion
Numerical analysis

ABSTRACT

The possibility to realize Additively Manufactured functionally graded lattice structure based on Voronoi tessellation enormously increases the possibility in tailoring the stiffness, mechanical properties and energy absorption capacity of the samples. The work presents the design and mechanical characterization of functionally thickness graded Voronoi lattice structures in comparison with constant thickness lattice structures for the evaluation of mechanical performance and energy absorption capacity. Firstly, the design and laser power bed fusion process are detailed. The dimensional deviation between designed models and Ti6Al4V specimens is quantified to assess the samples' quality. Their mechanical performance is analyzed by quasi-static compression experimental tests, supported by numerical analysis for the evaluation of local stress distributions and deformation modes. The average dimensional deviation between CAD models and fabricated samples is 0.09 mm, likeminded with the literature optimum. The structures exhibit Young Modulus values ranging between 10 MPa and 21 MPa, compatible with biomedical applications. The compressive force for thickness graded structures tends to increase up to densification, while uniform thickness structures present an almost constant value of force in the platform stage. Additionally, the energy storage changes according to the presence of thickness gradient: the larger the thickness gradient, the larger the energy absorption capacity.

1. Introduction

Cellular structures attract attention in different fields of interest, as they combine lightweight and good mechanical resistance, as well as interesting energy absorption [1] and heat dissipation ability [2]. The design of lattice structures has been encouraged by Additive Manufacturing (AM) technology: among the AM processes, laser powder bed fusion (LPBF) process is one of the most adopted [3]. Main metallic materials used in LPBF are titanium alloys, steel, aluminium alloys and NiTi [4,5] and main applications field include biomedical, aerospace and automotive industry [4,6–10].

For instance, in biomedical applications, porous structures can be employed in bone scaffold or included in the structure of orthopedic prosthesis to enhance the osteointegration [8,9]. In similar cases, lattice structures bring enormous advantages thanks to their large specific surface area which may improve the migration of bone cells and fluid flow [11], and pores with adequate dimensions promote bone in-growth and decrease the stiffness of the device with a consequent benefit in preventing stress shielding [12]. The apparent elastic modulus of human bone ranges from 10 GPa to 30 GPa and from 20 MPa to 1 GPa for cortical and trabecular bone, respectively [13], while titanium alloys, which are among the preferred materials owing to their biocompatibility and their consolidated success in orthopedic prosthesis fabrication [14], are much stiffer than bone in bulk conditions ($E = 100$ GPa): in this light, the introduction of a tailored porosity allows to reduce this gap [11]. As an unavoidable drawback, mechanical strength of a lattice structure is decreased by the introduction of pores. In automotive and aerospace field the thermal conductivity is a key feature for thermal management applications [15] and energy-absorbing capacity is crucial for handling vehicle collision and probe landings [4]. In similar applications, Ti6Al4V and NiTi are often promising materials to be chosen. Yu et al. [4] designed NiTi bionic lattice structures, which were demonstrated to be anti-shock structures with large energy absorption capacity owing to the superelasticity of employed material. Bai et al. developed Ti6Al4V

* Corresponding author at: Politecnico di Milano, Mechanical Engineering Department, Milano, Italy.
E-mail address: chiara.bregoli@polimi.it (C. Bregoli).

https://doi.org/10.1016/j.mtla.2024.102234
Received 22 May 2024; Accepted 10 September 2024
Available online 11 September 2024

LPBFed lightweight curving lattice structures characterized by no sharp nodes and enhanced energy absorption ability [7]. Beside the material choice, it is crucial to define the best porosity, providing the desired blend of low weight, elastic modulus and compressive strength, for a specific application.

Lattice structures can be classified into three categories: truss and node regular structures [16–18], triply periodical minimal surface (TPMS) [19,20] and stochastic structures [1,21,22]. The first type is the most studied and investigated, fabricated in different materials [23]; it includes structures consisting in the replication in space of a unit cell, e.g. a diamond cell, body centred cubic (BCC) cell, octahedral cell and so on. TPMS structures result from the assembly of several continuous surfaces with the possibility to control pore size, porosity and periodic unit cells [1], and are often chosen thanks to their smooth arrangement and absence of sharp profiles. Stochastic lattice structures can be designed by means of Voronoi-tessellation approach [24]: this type of open cell foam stochastic structures has recently attracted much interest [1,8,11]. Researches based on similar lattice structures are mainly focused on the biomedical field [8,11,25]: Du et al. fabricated porous Voronoi scaffolds, whose stiffness and compressive strength met the bone tissue requirements [11]; Herath et al. [8] employed the Voronoi tessellation for the realization of a bone-like scaffold meant for large bone defects.

Each of the above-reported types of lattice structures can be Uniform Lattice Structures (ULSs) or Functional Graded Lattice Structures (FGLSs) [21,26–30]. While in the former group the mechanical performances are uniform throughout the design domain, in the latter one the structure exhibits different mechanical properties along its volume: these changes are due to porosity gradient, obtained by means of struts length variation, gradient and combination of unit cells and struts thickness variation [26]. Wang et al. designed Ti6Al4V LPBFed FGLS stochastic lattice structures by changing struts thickness: the samples were fabricated for biomedical purpose and the registered mechanical performances fitted the cortical bone requirements [21]. Wang et al. addressed only an experimental mechanical characterization of the samples in the elastic region, without focusing on energy absorption capacity nor addressing computational stress and strain evaluation and without quantifying the dimensional deviation between CAD models and fabricated samples. On the contrary, Jagadeesh et al. employed truss regular structure, a BCC unit cell, and evaluated the energy absorption capacity of FGLS structures: gradient regular structures exhibited an improved energy absorption capacity, which could be beneficial for aerospace and biomedical implants [27,31].

Most of the studies available in literature deal with regular lattice structures, while far smaller attention has been devoted to stochastic ones. In this respect, the possible advantages of a graded design over a uniform one still need to be addressed: the relationship among design input, porosity, LPBF processability and related mechanical properties are still under debate and may require considerable efforts. A successful development in this field would allow to tailor elastic modulus and energy absorption, according to the specific needs of each application [11,21].

In the present work, Ti6Al4V Voronoi ULS and FGLS lattice samples with longitudinal thickness gradient are designed and realized by LPBF in order to compare their mechanical behaviour in relation with processability, porosity and energy absorption capacity, by means of both experimental and computational analysis. Firstly, the designs are optimized and realized with previously consolidated process parameters. Thereafter, both surface and volume morphological analysis is carried out for the assessment of processability by measuring the dimensional mismatch between fabricated samples and designed models. Then, quasi-static experimental compression tests are performed and discussed with the help of finite element analysis (FEA). The Young moduli of all structures are compatible with bone stiffness making the structures promising for biomedical applications. Despite the thickness gradient and the stochastic struts distribution, a strong linear correlation between Young moduli and relative density is observed. The introduction of a longitudinal thickness gradient in FGLS improves the energy storage ability, especially at high strain values; on the contrary, ULS samples, despite the stochastic Voronoi arrangement, registered an almost constant energy storage during the increasing the strain.

2. Materials and methods

2.1. Voronoi tesselation design

Firstly, a cylinder with diameter of 10 mm and height of 15 mm is designed by CAD (Computer Aided Design) software (Inventor, Autodesk, USA): the cylindrical region represents the outer volume of the porous structure. Secondly, this volume of interest is imported in 3-matic software, where the Voronoi tessellation is created (3-matic, Materialise, Germany) [32]. The Voronoi diagram is a mathematical subdivision of space and it results in a graphical lines representation in the 3D space which requires specific input for the design of the thickness and strut section, such indicated in [21]. Target maximum pores size, minimum and maximum thickness are set as input parameters, thus producing five conditions (Table 1), whose CAD models are reported in Fig. 1. Five different models are designed: one ULS model with constant thickness equal to 0.5 mm to be compared with four FGLSs which thickness changes longitudinally the entire specimen, as indicated in Fig. 1.

It is worth noting that in regular lattice structures usually a minimum number of cells is recommended in lattice structures design for the minimization of possible surface effects on mechanical performance consistency and reliability [33]: however, the current manuscript aims precisely to focus on the mechanical characterization of small lattice structures with large pores which could be implemented in industrial and biomedical field. Additionally, no “regular cells” is present in the proposed Voronoi tessellation: the possible surface effects on mechanical performance which may due to the small dimension of samples in comparison with the designed large pores dimensions are balanced by the cylindrical shape of the specimens and the connections among struts which make repeatable and reliable obtained mechanical performance, as confirmed by the experimental results in the Results section. Secondly, the few researches on large pores lattice structures do not considered a minimum number of “cells” [8,34]. Finally, both surface and volume of the bounding cylinder is considered in the design of Voronoi lattice structure: these choice results in the fact that the external struts are interconnected each other providing a sort of boundary of the entire lattice structure on the contrary respect to what is designed in Wang et al. [21] in which no external connections are provided among the struts branches.

CAD surface, CAD volume, CAD mass and CAD porosity are calculated for each of the five models.

The average CAD porosity of each model is calculated by considering the stl file (1).

$$\text{Average CAD Porosity} = \frac{\text{Volume}_{\text{bounding cylinder}} - \text{Volume}_{\text{CAD lattice strcuture}}}{\text{Volume}_{\text{bounding cylinder}}} \times 100 \quad (1)$$

Table 1
Input parameters of the designed models.

	ULS	FGLS			
	REG	GRAD25	GRAD50	GRAD75	GRAD100
Minimum thickness (mm)	0.5	0.5	0.5	0.5	0.5
Maximum thickness (mm)	0.5	0.625	0.75	0.875	1
Target maximum pores size (–)	2	2	2	2	2

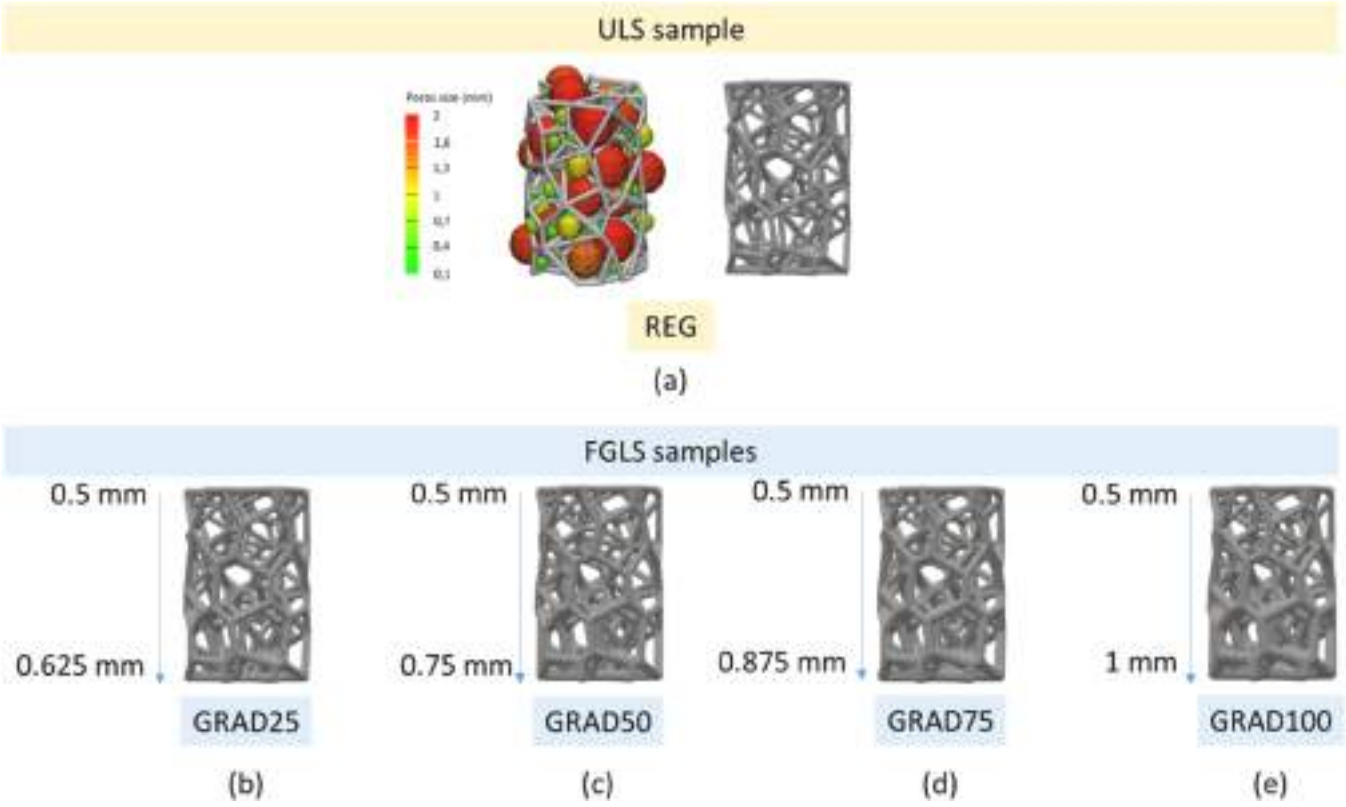

Fig. 1. pore size analysis reported for REG sample. Target maximum pore size is equal to 2 mm; average pore size is equal to 0.71 mm. Similar inputs are for FGLS samples. CAD model for REG (a); CAD models for FGLS samples (b–e).

Despite the samples have in common the starting Voronoi tessellation diagram, the 3D struts arrangement is evaluated by the measurement of the degree of anisotropy (DA) and connectivity density (Conn_D) obtained by means of ImageJ software by means of BoneJ, a plug-in for bone image and bone-like image analysis [33]. Firstly the stl file is sliced and thereafter the set of slices of each sample is used as input in ImageJ software [35]. DA defines the 3D space orientation of struts, which can be isotropic (DA→0) or anisotropic (DA→1). DA assessment allows to evaluate the isotropic orientation of the struts [36]: since in the current manuscript, no specific orientation of the struts is considered, a DA close to 0 is expected. Further additional analysis should be focused on the impact of the struts orientation on the mechanical performance of similar complex Voronoi lattice structures. Conn _D evaluates the number of connected struts per volume unit and it provides helpful information of the struts arrangement [36,37]. It is worth noting that Conn_D may be affected by the thickness of the close struts which, if thicker, may make two close struts collapsed in a single one, with a consequent impact on Conn_D value.

2.2. Samples fabrication

An LPBF system (mod. AM400 from Renishaw), equipped with a pulsed wave laser was used to produce lattice structures using medical grade Ti6Al4V powder. The used processing parameters, which were optimised in a previous work [38], allowed to achieve relative densities in excess of 99.7 % and are reported in Table 2. Firstly, five replicas of tensile samples are realized to evaluate the mechanical properties of the bulk material. Thereafter, each lattice model is produced with both their main axis and, for gradient structures, the direction of increasing density perpendicular to the building platform (Fig. 2). Three replicas of each model is realized for the experimental evaluation. All specimens are subjected to a heat treatment at 850 °C for 1 h under high vacuum and then naturally cool to room temperature.

Table 2
LPBF process parameters used to produce Ti6Al4V samples.

Parameters	Values
Scanning strategy	Meander
Laser spot size [μm]	65
Hatch spacing [μm]	65
Point distance [μm]	75
Layer thickness [μm]	30
Power [W]	200
Exposure time [μs]	50

2.3. Forming quality characterization

MicroCT scans are performed for the evaluation of the geometrical and dimensional mismatch between fabricated specimens and designed models. For MicroCT imaging, a ZEISS machine (Xradia Context MicroCT, ZEISS, Germany) with a current of 126 μA and an exposure time of 0.75 s is employed. Samples are scanned with a voxel size resolution of 16 μm. The obtained tomography datasets are reconstructed using Dragonfly software (Comet Technologies Canada Inc.), and the 3D distribution of dimensional mismatch in the samples is determined using Dragonfly's segmentation toolkit. Scanning Electron Microscope (SEM Leo 430 by Zeiss) observations are useful for the evaluation of the AMed typical surface.

2.4. Experimental analysis: tensile tests and quasi-static compression tests

Tensile tests and quasi-static mechanical compression tests are performed with a MTS exceed E45 and MTS 2/M machine, respectively (MTS System Corporation, USA). Tensile tests are carried out on dog-bone specimens following ASTM E8 standard at strain rate 0.015

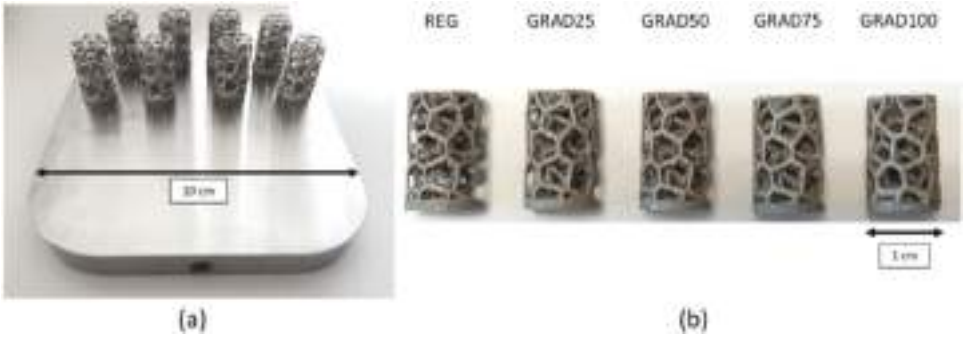

Fig. 2. As-fabricated Ti6Al4V components: example of one of the printed building platform (a); comparison between designed models and fabricated ones (b).

min^{-1}. Material mechanical properties are thereafter used as input for the definition of material constitutive model applied in the numerical analysis.

Compression tests on ULC and FGLSs are carried out at strain 0.05 min^{-1} according to ASTM E9 standard (Fig. 3a). Compression tests are terminated at 50 % strain (7.5 mm of displacement), where the structure already entered in the densification stage [39]. Compression force–displacement curves are converted into engineering stress - strain curves, based on the nominal dimension of the specimens as if it were a dense part, as widely accepted and explained in Gibson–Ashby model [40]. Apparent stiffness, peak force, energy absorption at different strain levels/displacement, strain energy absorption (E_a) and specific energy absorption (SEA) are the main properties measured for each specimen.

E_a can be computed according to the following Eq. (2):

$$E_a = \int_0^{\varepsilon} \sigma(\varepsilon)\, d\varepsilon \ \left[\ \mathrm{J}/\mathrm{mm}^3\right] \tag{2}$$

where $\sigma(\varepsilon)$ and ε represent the engineering stress and strain at which the absorbed energy is calculated. Specifically, both the global absorbed energy and intermediate absorbed energy at different steps are calculated.

SEA is defined as the energy absorbed per unit mass of the structure and represents the structure utilization efficiency of energy absorption [41].

$$SEA = \frac{\int_0^l F(x)\, dx}{m} \ \left[\ \mathrm{J}/\mathrm{g}\right] \tag{3}$$

where m is the total CAD mass of the structure obtained from .stl file and l is the displacement up to which the SEA is measured. Deformation and failure modes are also captured by a video camera and visually evaluated for each sample.

2.5. Numerical analysis of the mechanical response

The deformation behaviour and stress distribution of the ULS and FGLSs are evaluated by Abaqus Implicit software (v2017, SimuliaTM, Dassault, Germany). Elastoplastic material model is chosen and calibrated with Ti6Al4V properties obtained from tensile tests (Fig. 3): experimental strain hardening is considered and implemented in the simulation. A Von-Mises plasticity-based material model (plastic in Abaqus CAE 2017) is chosen for the trabecular specimens, whereas a ductile damage failure model is used to model the fracture of the samples (Fig. 3). Tetrahedral adaptive quadratic mesh (C3D10 – second order) is adopted in 3-matic software (3-matic, Materialise, Germany). The chosen element size to guarantee numerical convergence for each sample is 0.05 mm (Fig. 4a). The model is sandwiched between two rigid plates with the following boundary conditions: in the simulation the bottom side is immobilized, while the upper one is moved downwards up to 10 % strain (Fig. 4b and c). The contact among the up moving rigid plate and structure is hard frictionless surface-to-surface contact. The influence of strain rate is not considered during the quasi-static compression simulation. During job execution, the parallelization of the FEA is undertaken by 8 processors (Intel(R) Core(TM) i7–10850H CPU @ 2.70 GHz 2.71 GHz).

3. Results

3.1. Dimensional and geometrical qualification

CAD parameters obtained from the analysis of each .stl file and struts arrangement data are reported in Table 3. The porosities, resulting from the design choice, range from 77 % up to 88 %, which is considered the best range stated for biomedical application [10,42]. MicroCT images are used to obtained data on struts arrangement. The stochastic struts

Parameter		Values
Material constitutive model	E [GPa]	100
	ν	0.3
	σ_y [MPa]	800
Ductile damage model	Fracture strain	0.13
	Stress triaxiality	0.25
	Strain rate	0

(a)

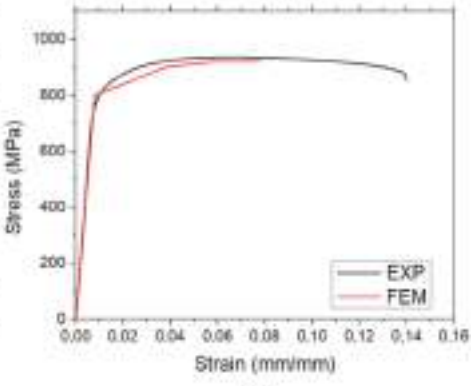

Fig. 3. Input parameters for the material model (a); exp vs. fem curve of material model (b).

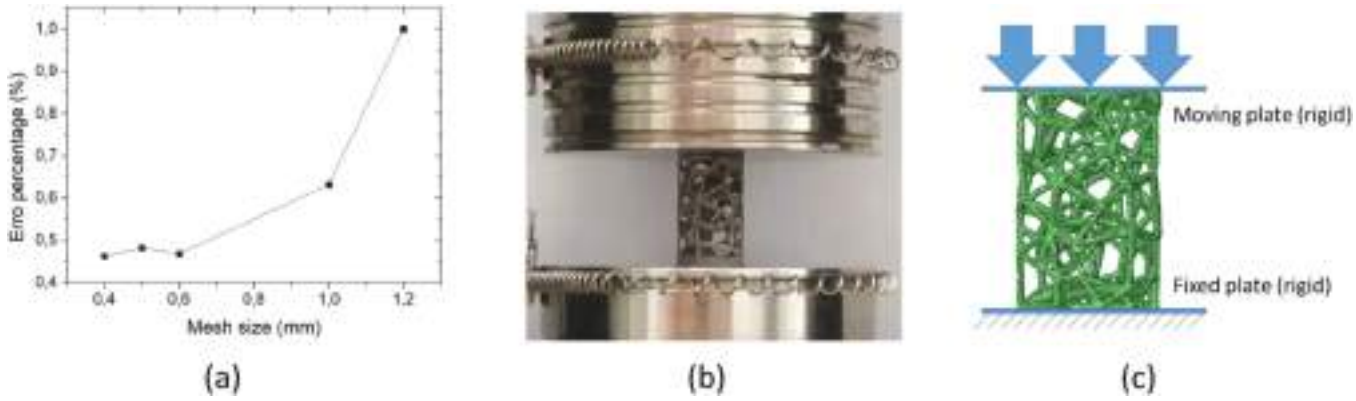

Fig. 4. Mesh convergence (a); quasi-static compression: testing machine (b); FEA model (c).

arrangement is highly isotropic (DA → 0) and similar for all specimens, since the input parameters for the struts orientation is the same. The Conn_D is around 2.9 ± 0.2 mm^{-3} which means that about 3 struts are interconnected in a volume of 1 mm^3. The slight differences in the Conn_D is due to the fact that, by increasing the struts thickness in struts very close each other (smaller pores size) lead to fusion of such neighboring small struts. In conclusion, the results confirmed that all fabricated LPBFed samples share a similar 3D struts arrangement, as required from the design input and set in the design models.

The surface morphologies of fabricated ULS and FGLS models are shown in Fig. 4. There are partially melted particles attached on the surface, as widely demonstrated in the literature [43]. Moreover, the presence of staircase effect is another geometrical error typical to AM processes, such as LPBF [44].

According to the dimensional assessment, as anticipated by SEM images (Fig. 5), the struts exhibit a deviation from the CAD model: the dimensional mismatch between fabricated samples and designed models is quantified in Fig. 5.

The maximum measured dimensional deviation is around 0.7 mm (Fig. 6), while the distribution map shows that the average dimensional deviation is about 0.09 mm. This dimensional deviation corresponds to 18 % for ULSs REG, where the CAD struts thickness is constant at 0.5 mm. Conversely, the average dimensional error ranges between 9 % and 18 % in FGLSs, where the thickness varies along the specimens. Despite the error percentage looking big, it shall be underlined that it is localized in specific regions of the samples: indeed, greater deviation occurs in thinner struts, that are inclined with respect to the building direction. Nodes do not present significant dimensional deviation. The observed distributions of dimensional deviations are similar in all samples, as reported in Fig. 6.

Generally speaking, the greater dimensional deviation occurs in the upper inner walls of the holes and on the down facing surfaces, where particles tend to drop because of gravity, as reported in literature [45,46] (Fig. 7). It is worth reminding that surface finishing is not considered in the current work: however, a surface finishing would have most likely minimized the discrepancies between CAD and real samples. 2D slice images clearly show the presence of partially adhered powder on the down-skin face of tilted struts (Fig. 7c). The low dimensional deviation and good quality of samples confirm that the suitable process parameters, positioning in the building platform and scan strategy were chosen.

3.2. Mechanical testing

The typical compression force-displacement curve obtained under compression for porous materials is observed for regular ULS samples (Fig. 8a): a first linear-elastic stage is followed by a force plateau related to plastic deformation and a final densification region, which leads to increased stiffness and strength due to the contact among struts themselves [44,47]. The final densification area occurs when the lattice structures are completely compressed as indicated in Fig. 10 at the last step [48]. In stretch-dominated lattice structures a first peak of force is reached and then deformation occur with an oscillating force [44]. This sequence holds for REG ULSs as well, despite the absence of a regular unit cell. On the contrary, FGLSs exhibit an initial linear-elastic stage (up to 0.5 mm of displacement), then, instead of going through an extended plateau, force drops to a minimum (at about 1–1.5 mm of displacement), and finally starts to increase again up to densification. The increase in force in the middle area (between 2 mm and 6 mm of displacement) becomes more evident as the thickness gradient gets higher (Fig. 8a). Densification occurs at 7 mm of displacement (about 45 % of strain) for all samples but GRAD100, which exhibits densification at 6 mm of displacement (about 35 % of strain). The densification phase in GRAD100 occurs for smaller displacements due to the greater thickness of the struts. FGLSs, due to the presence of thickness gradient, exhibit a mechanical behaviour which cannot be labelled as strictly bending-dominated nor stretch-dominated, but turns out to be a combination of both with the addition of the buckling effect, which occur in the vertical structures. In the presented the lattice structures both slender and less slender struts are present: since buckling strongly depends on the slenderness of the struts, it occurs mainly on the slender struts, as reported in the figures [37].

Fig. 8b shows the experimental stiffness values (N/mm) measured in the first linear-elastic stage for each sample. Average values of stiffness and standard deviation are summarized in Table 4. ULSs exhibit the lowest stiffness, related to its high porosity (88 %, Table 3), while FGLSs show greater stiffness values, progressively growing according to a

Table 3
CAD parameters and struts arrangement data obtained from BoneJ.

	Samples	REG	GRAD25	GRAD50	GRAD75	GRAD100
CAD parameters	CAD surface [mm^2]	9060	10,051	10,405	10,916	11,355
	CAD volume[mm^3]	131	178	200	240	282
	Average CAD porosity [%]	88	85	83	80	77
	CAD relative density (1-porosity) [%]	12	15	18	20	23
	CAD mass [g]	0.58	0.78	0.88	1.06	1,24
Bone J indices	DA [-]	0.23	0.22	0.19	0.2	0.17
	Conn_D [mm^{-3}]	2.7	3.2	3.1	3.0	2.9

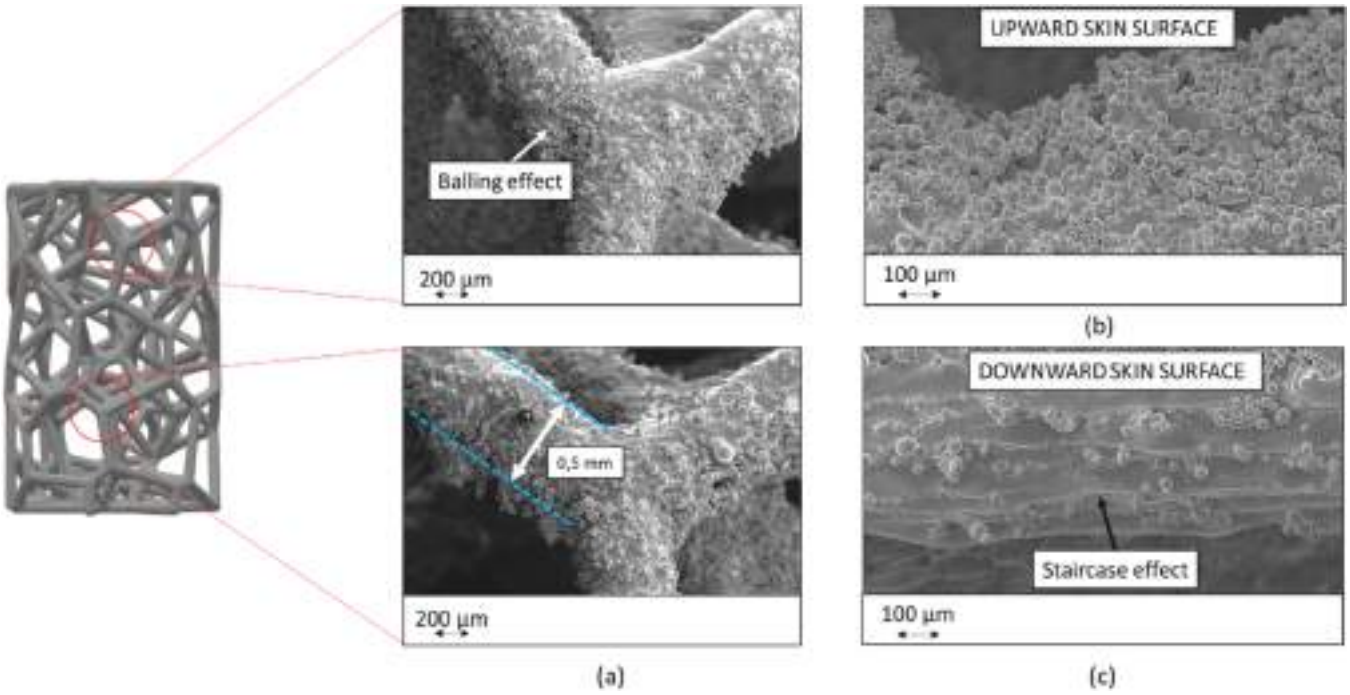

Fig. 5. SEM images referred to GRAD 25 sample: same observations are obtained from the analysis of other fabricated samples. Blue dot lines indicate the ideal CAD profile which is smaller than the fabricated ones (a); upward skin surface (b); downward skin surface (c).

linear trend. The corresponding values of Young moduli, calculated by considering the nominal section of each sample, are reported in Table 4. Such values, which range between 10.5 MPa and 21.4 MPa, meet the requirements of bone-like structures making the designed Voronoi lattice structures promising for biomedical prostheses, as suggested in [13].

Fig. 8c presents the first peak compressive force of each sample. REG ULS samples exhibit the lowest peak force equal to 1252 ± 13 N, followed by the FGLSs. As the relative densities of different FGLSs linearly increases from 25 % to 100 %, the peak forces of the samples increase accordingly: the greater is the longitudinal gradient, the greater is the peak force. Indeed, GRAD25 FGLSs show a peak force of 1851 ± 62 N, while GRAD100 FGLSs show a peak force of 2786 ± 126 N. Moreover, the peak force of GRAD100 FGLSs is almost double the peak force registered for the REG ULSs. Secondly, while the average difference between the peaks force in FGLSs among the neighboring samples is around 300 N (difference between GRAD25-GRAD50, GRAD50-GRAD75 and GRAD75-GRAD100), the difference between the first peak force in REG ULSs and GRAD25 FGLSs is almost double, equal to 599 ± 49 N (Fig. 8d): consequently, it is possible to state that the introduction of a thickness gradient strongly affects the peak force (by doubling peak force value), while the peak force slightly increases by the same value (about 300 N) by increasing the gradient. Although the peak force values of various samples are different, they occur mainly in the same range of strain, as indicated in Table 4.

As previously explained in Table 3, in the analyzed designed structures, the relative density changes by changing the thickness gradient (i.e. the relative density is not kept constant among the specimens) and the obtained mechanical performances are therefore influenced by all these aspects: since the impact of relative density is already well known in the literature, it is necessary to observe if and how the only gradient itself lead a contribution in the results. As depicted in Fig. 9b, it is worth noting that, the trend peak force vs. porosity gradient differ from trend mass vs. porosity gradient, confirming the contribution of thickness/porosity gradient in the measure of peak force ($R^2 = 0{,}99$) (Fig. 9a).

Secondly, it is well known that according to Ashby, the relative Young modulus ($\frac{E*}{E_s}$) and relative density ($\frac{\rho*}{\rho_s}$) are linked by the following equation [37]:

$$\frac{E*}{E_s} \propto C1 * \left(\frac{\rho*}{\rho_s}\right)^n \quad (4)$$

where $E*$ and $\rho*$ are the Young modulus and the density of the lattice structures, E_s and ρ_s are the Young modulus and the density of the solid of which the lattice structure is made, C_1 is the Gibson-Ashby coefficient which depends on topology and materials and n is the exponent which depends on configuration of struts relative to loading direction [37,44].

Fig. 9b shows the Gibson-Ashby plots in log-log diagrams for experimental Young modulus for FGLSs by considering their average porosity [44].

It is well established that usually lattice structures exhibit a linear correlation between the two variables in a log-log plot, as indicated in [37,44]. In the current research, firstly, the relative Young modulus and the relative density are calculated, then the results are compared with results presented in Maconachie et al. [48]: the results of the present manuscript related to a stochastic lattice structures, such as Voronoi lattice structures are, seem overlapping the results obtained by Maconachie et al. for regular lattice structures (such as BCC, diamond, FCCS, and so on). In the current evaluation, it is remarkable that, despite the stochastic struts arrangement and the longitudinal thickness gradient (i.e. porosity gradient), a linear correlation between the two variables is still observed ($R^2 = 0.95$). The values of constants C and n are reported in the graph (Fig. 9b) (C = 0.0013 and $n = 1{,}2$).

The video frame images showing the deformation and fracture of ULSs and FGLSs are compared in Fig. 10. Five characteristic displacement values are considered in the images.

The mechanics of collapse of all samples shows a combination between shear-mode and layer-by-layer mode: the shear fracture is consequent to the stochastic arrangement of struts, while the layer-by-layer fracture is related to the density gradient. Moreover, buckling collapse may occur in vertical struts parallel to the direction of applied load.

REG ULS samples show an initial collapse in the bottom region followed by a uniform collapse of the entire structure (Fig. 10a). A shear

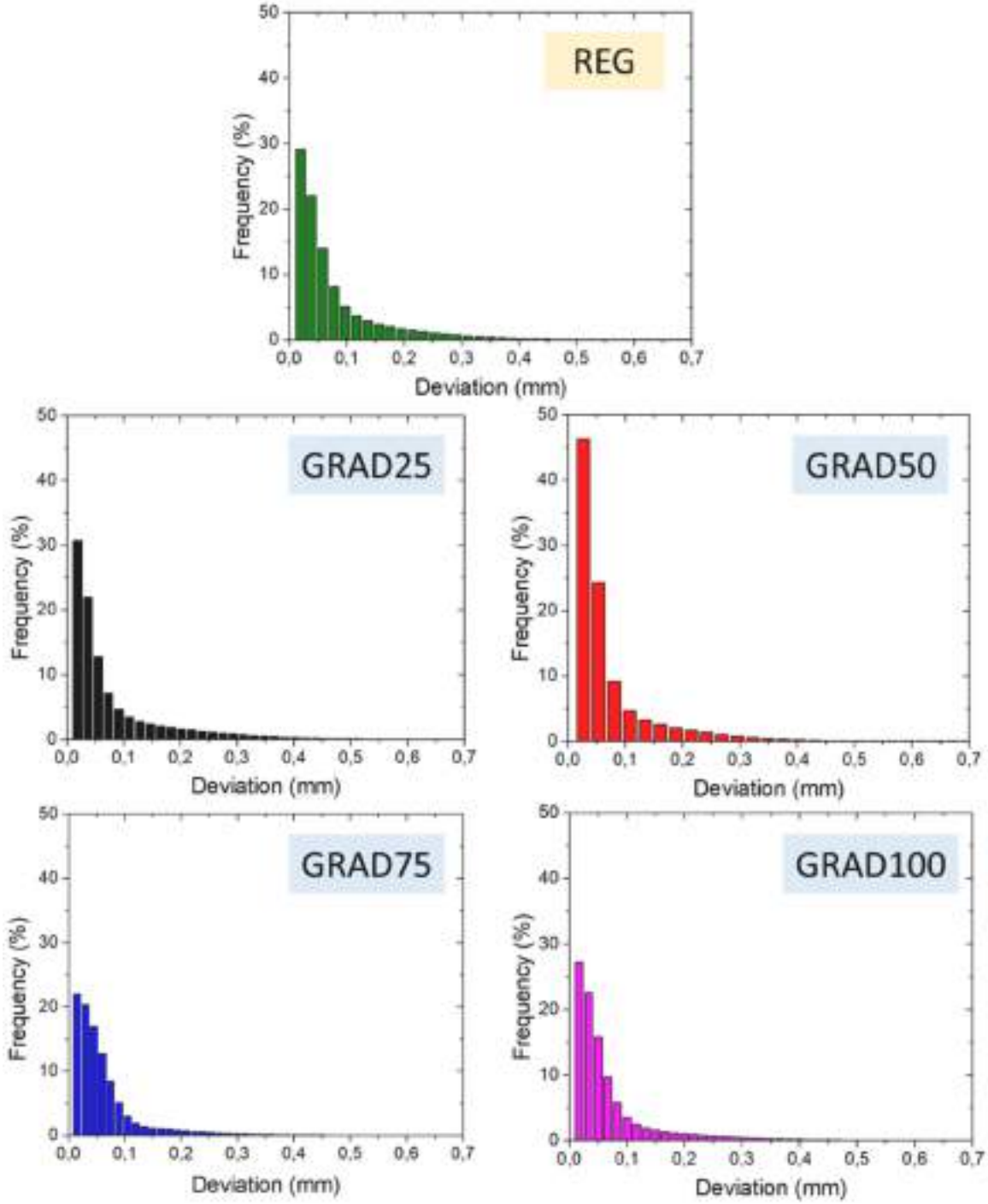

Fig. 6. frequency of dimensional deviation expressed in mm and obtained from the segmentation in Dragonfly.

fracture is evident in the stress distribution (see numerical analysis). The FGLSs exhibit mainly a layer-by-layer fracture: they show an initial collapse in the upper region of the samples, which is the low-density region; thereafter, such upper layer densifies when displacement increases, and the collapse extends to bottom layers where density is higher. Such layer-by-layer fracture behaviour is evident in GRAD25 samples, which presents a low strut thickness gradient, and the entire sample contributes in load bearing. However, samples with the greatest density gradient (GRAD100), present a significate difference in strut thickness between the top and bottom parts; therefore, the collapse is mainly confined in the upper part and hardly propagates to the area characterized by thicker struts.

The main drops in force highlighted in Fig. 8a occur mainly when displacement reaches 6–7 mm and after the extended plateau and they correspond to the collapse and fracture of the most stressed struts: in Fig. 10 some pieces of struts are circled. Finally, densification occurs when displacement is about 7 mm for GRAD25, GRAD50 and GRAD75, while GRAD100 FGLSs experience an earlier densification when displacement is about 6 mm. Densification occurs at different values of displacement because the thicker the bottom struts are, the less they deform; therefore, load is borne by the upper thinner struts only, as occurs in GRAD100.

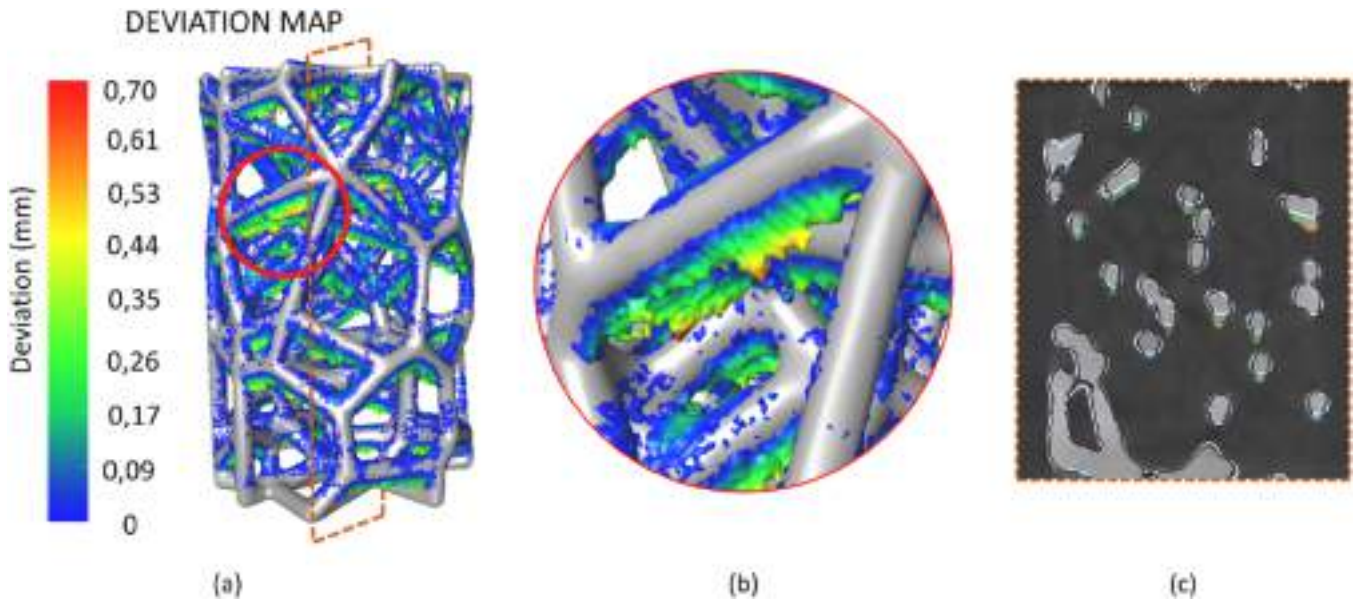

Fig. 7. Deviation map for GRAD75 (a); detail of down-facing surfaces, where deviation is the greatest (b); 2D slice, in which the down-facing surface and the mismatch between CAD contour (black and coloured contour) and sample's mesh contour (white contour) is evident (c). Similar results are obtained for all samples.

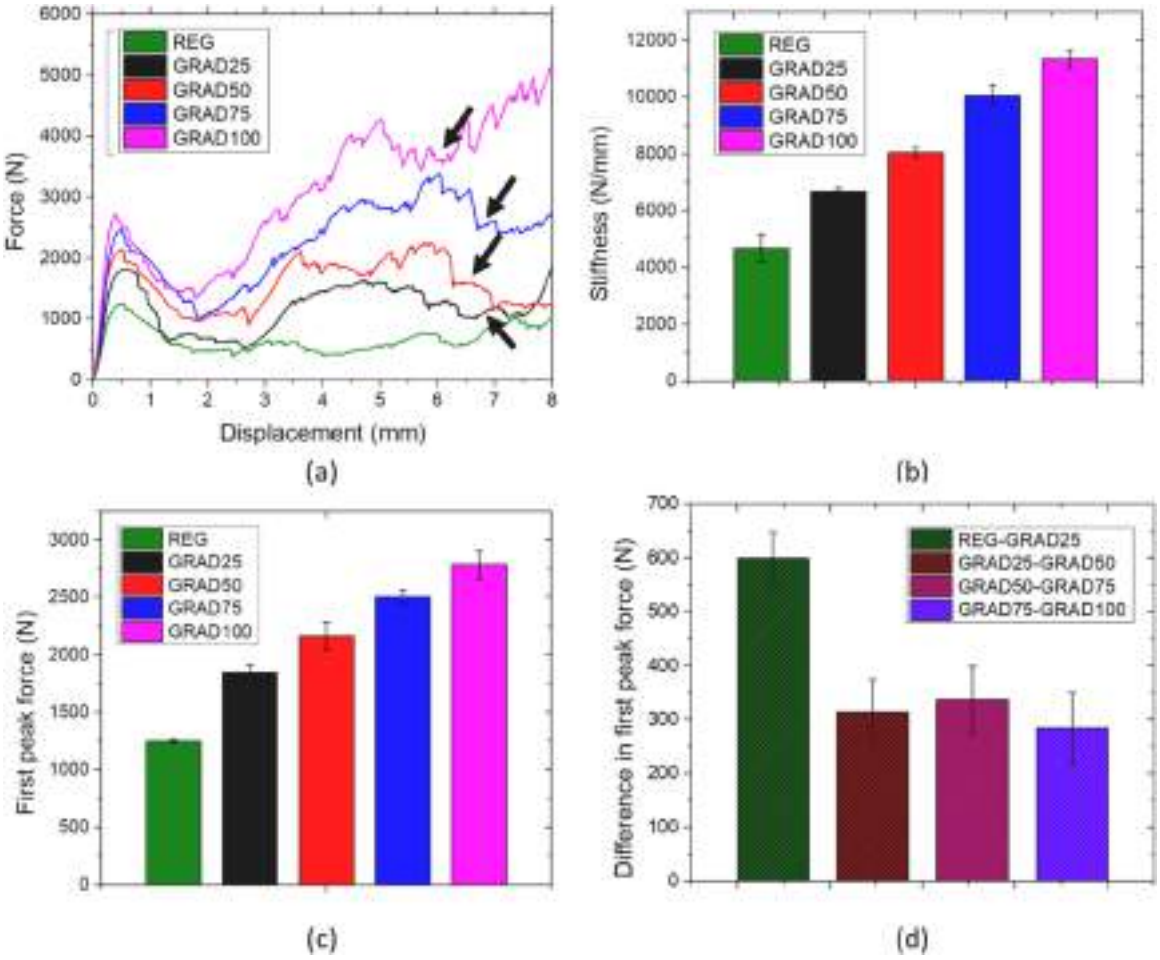

Fig. 8. Representative compression force-displacement curves for ULSs and FGLSs. Main drops in load are pointed out by black arrows (a); stiffness measurements (b); value of force at the first peak (c); difference among first peak force (d).

Table 4
Peak force and strain measured at the peak force for each sample, experimental stiffness and Young modulus.

	Sample	Peak force [N]	Strain at PF [%]	Stiffness [N/mm]	Young modulus [MPa]
ULS	REG	1252 ± 13	3.1 ± 0.1	4680 ± 502	10.5 ± 0.8
FGLS	GRAD25	1851 ± 62	3.5 ± 0.3	6680 ± 133	13.4 ± 0.7
	GRAD50	2165 ± 122	3.6 ± 0.4	8046 ± 161	15.3 ± 0.5
	GRAD75	2502 ± 60	3.1 ± 0.1	10,065 ± 352	20.7 ± 2.0
	GRAD100	2786 ± 126	2.5 ± 0.4	11,340 ± 330	21.4 ± 3.1

3.3. Energy absorption performance

Fig. 11 shows the results, related to the evaluation of the energy absorption ability displayed by the considered structures upon compressive deformation. The minimum total E_a is registered for ULSs, while for FGLSs, the greater is the gradient thickness, the greater is the amount of energy absorbed: indeed, the maximum total E_a is measured for GRAD100 FGLSs (Fig. 11a). As reasonable, E_a progressively increases with increasing strain (Fig. 11b). It may be observed that each curve presents a different slope, indicating that the structures are able to absorb energy at different rates, which result in a different performance of the lattice structure. In particular, the ULSs present a plateau area between 10 % and 30 % of strain, where the absorbed energy does not increase appreciably, while an evident increase in the absorbed energy takes place in the same strain interval for the graded structures.

For a better understanding of the dependence of energy absorption on strain, four areas of strain are defined: area 1 from 0 to 1.5 mm (0–5 % of strain), area 2 from 1.5 mm to 3 mm (5–15 % of strain), area 3 from 3 mm to 4.5 mm (15–25 % of strain), area 4 from 4.5 mm to 6 mm (25–35 % of strain). The last densification area (35–50 % of strain) is neglected. ULSs show a constant behaviour, absorbing the same amount of E_a, about 0.68 J/mm^3, in each area. FGLSs exhibit a different trend: indeed, E_a increases by moving to the next area, i.e. by increasing the deformation.

The E_a per CAD volume is graphed in Fig. 11d: a strong correlation ($R^2 = 0.99$) is evident between E_a and CAD volume. Despite a strong correlation is exhibited by the observation of all samples, the structures with the greatest CAD volume, i.e. GRAD100, the trend looks changing slope and a stiffer correlation occurs.

The CAD mass values summarized in Table 3 are used to calculate the SEA (Fig. 11e). FGLSs with the greatest gradient (GRAD100) have the largest SEA (24.6 kJ/g), followed by the FGLSs with inferior thickness gradients. REG ULSs have the lowest SEA (2.5 kJ/g). It can be state that FGLSs exhibit higher energy absorption capacity than ULSs: among the FGLSs, GRAD100 show the highest energy absorption capacity.

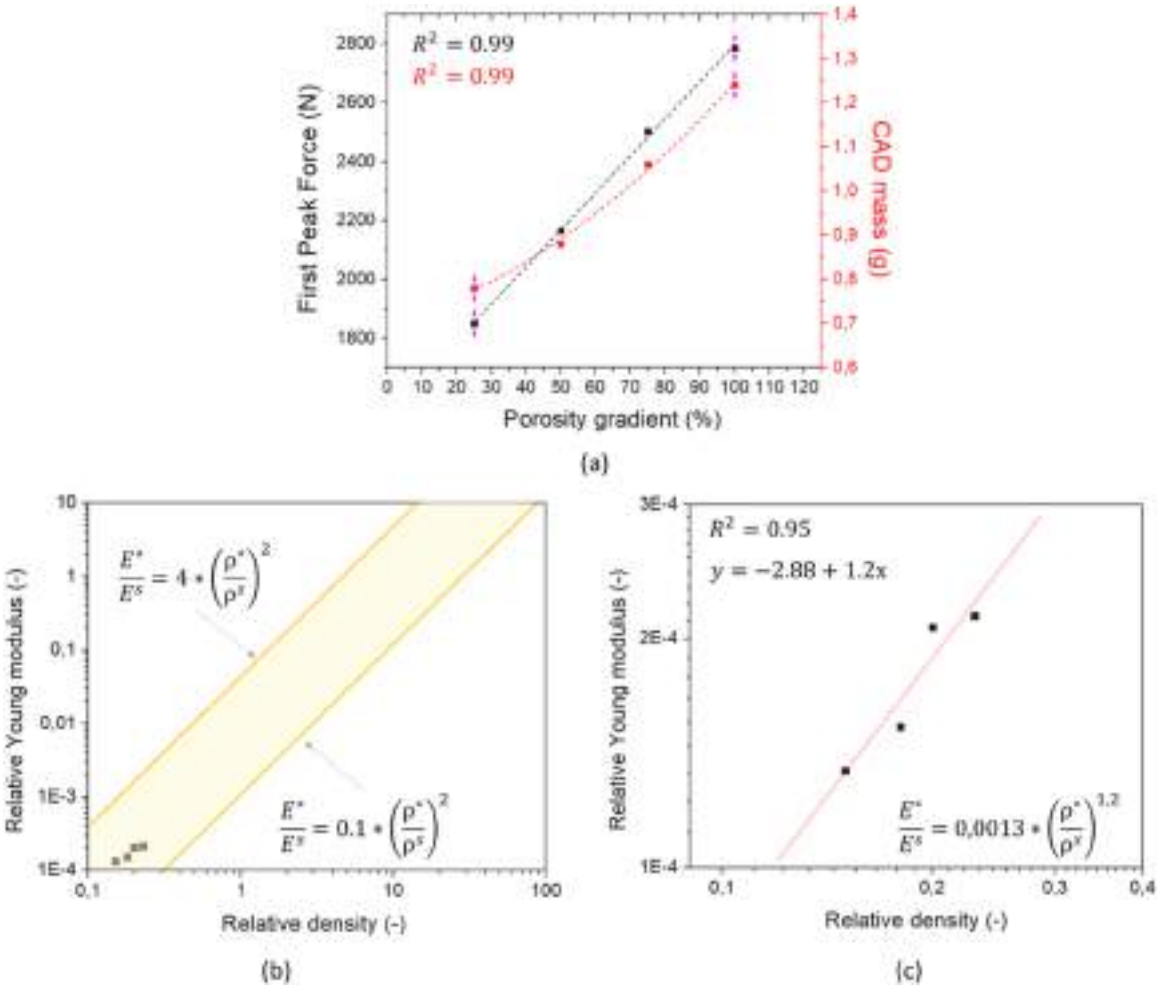

Fig. 9. Relation between peak force vs. porosity gradient (first order) and CAD mass vs. porosity gradient (second order) in order to assess the impact of different relative density (which leads to different mass values) and porosity gradient (a); relation among the results obtained for Voronoi lattice structures, compared with literature results [48] (b); focus on Voronoi lattice structure which exhibit a linear correlation between the two variables ($R^2 = 0.95$) (c).

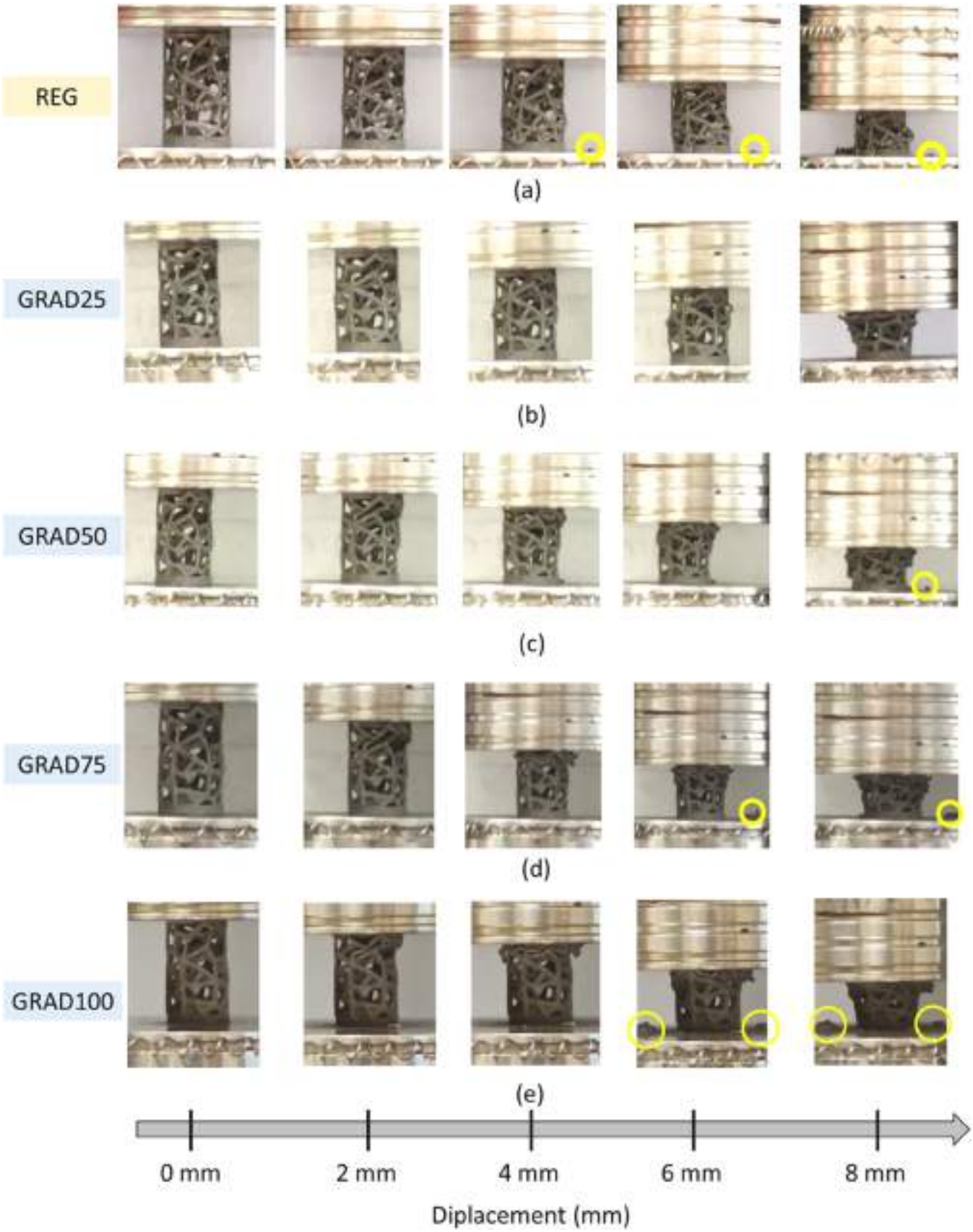

Fig. 10. Mechanism of collapse for each samples at different displacements. The yellow circles point out the broken struts.

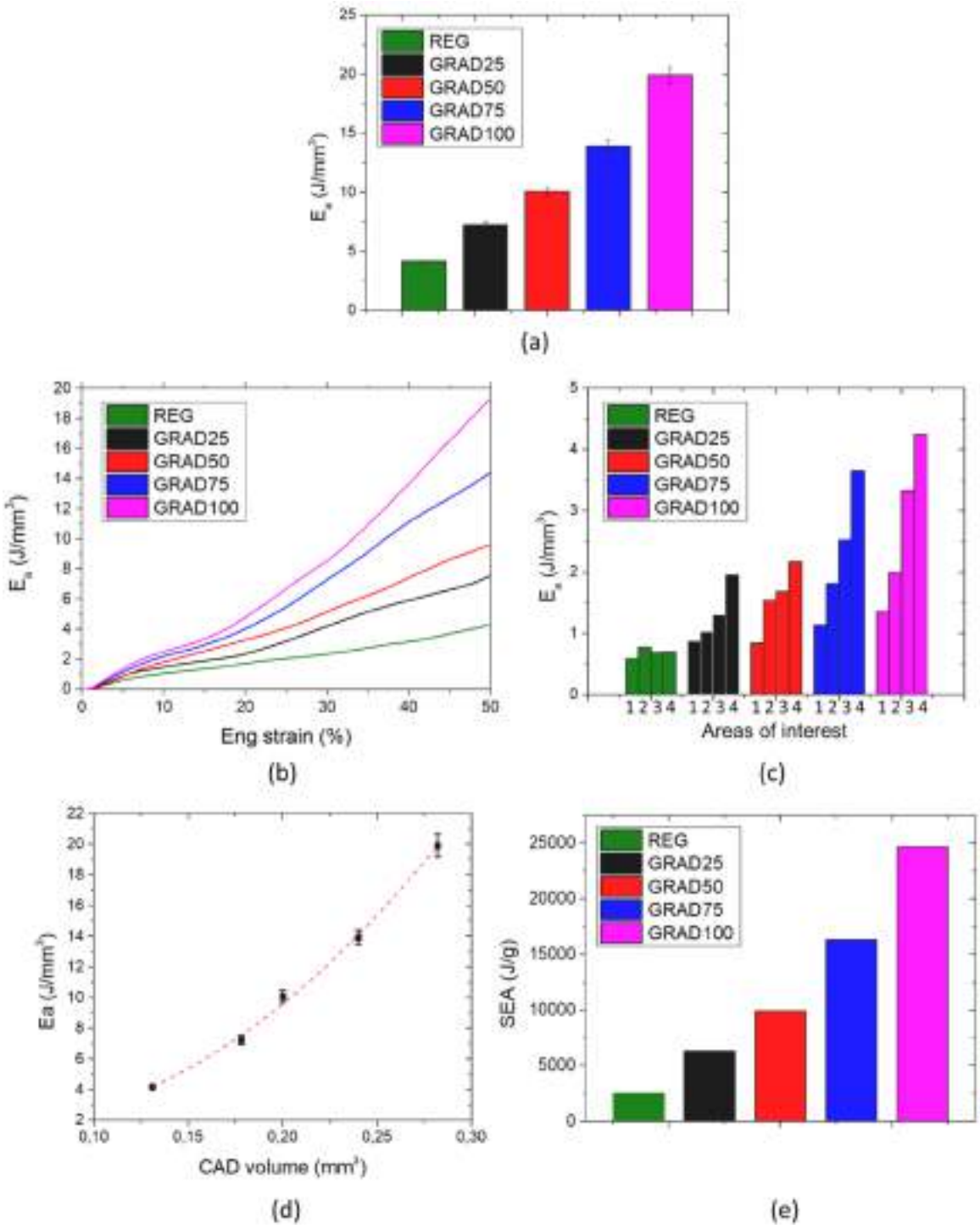

Fig. 11. Total energy absorbed by each structure (μ ± σ) (a). Energy absorption efficiency related to strain (b). Energy absorbed at different level of strain, i.e. in different areas (c). Energy per ideal volume (d). SEA for the different LBV structures (e).

3.4. Numerical analysis

The numerical analysis of the compressive behaviour of ULS and FGLSs models is conducted to quantify the effect of strut thickness gradient on stress distribution and deformation mode, with a particular attention on connections among struts. The FEA is carried out up to the first force peak, which means up to 1 mm of displacement (strain of about 6 %), i.e. in the area, which precedes the failure of first struts. In order to verify the quality of simulations, numerical force-displacement curves are compared with experimental ones: as shown in Fig. 12 numerical and experimental curves exhibit a similar trend in the region of interest.

As above reported, the dimensional deviations from CAD models observed in fabricated samples are repeatable in all samples: in the current simulations, they can be considered as a repeatable variation equal for all samples and thus neglected. The slight mismatch between experimental and computational curves observed in Fig. 12 can be attributed to the small geometric deviation and the intrinsic features of the computational model, as detailed below.

Numerical stiffness values are slightly higher than the experimental

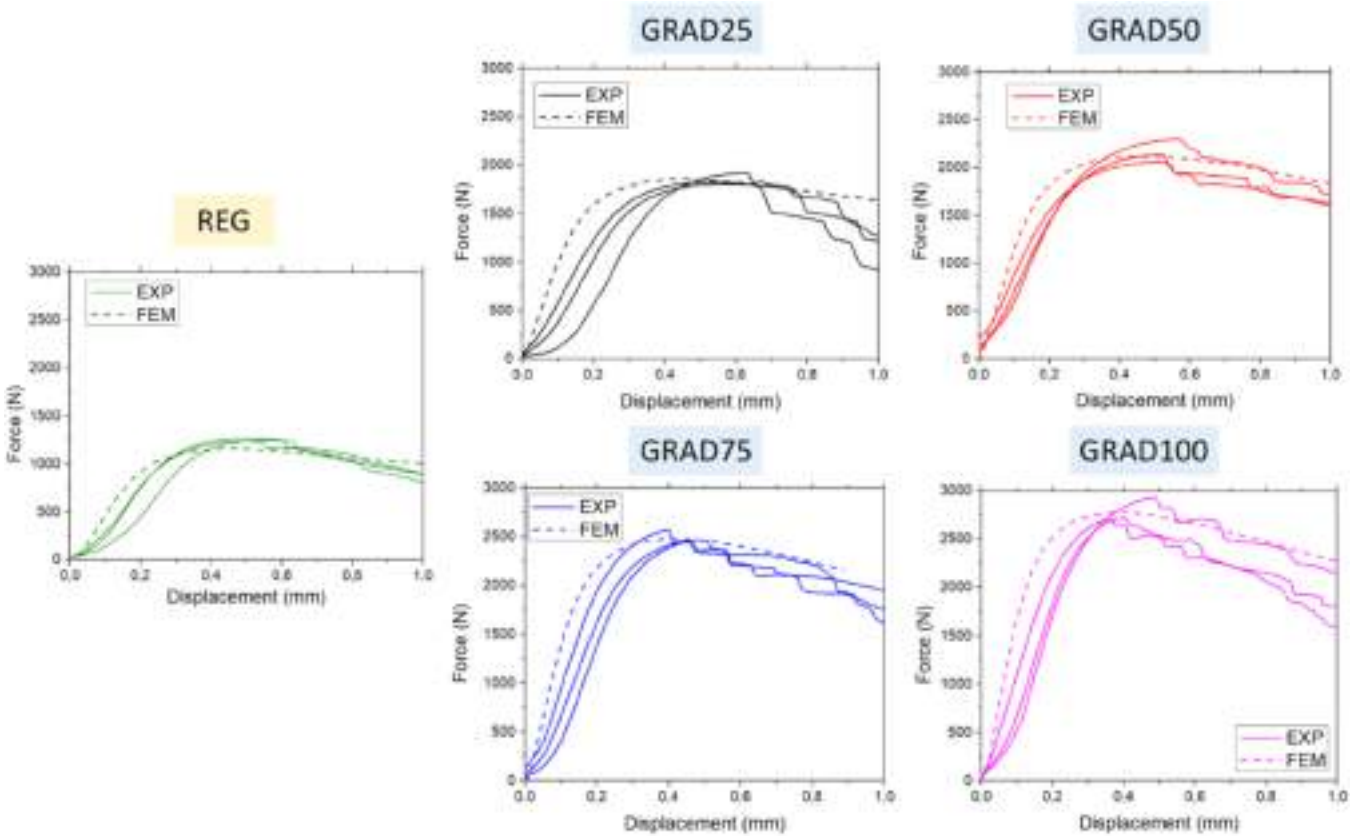

Fig. 12. Force-displacement curves: experimental results (continuos lines) vs. numerical results (dotted lines).

ones: these discrepancies between experimental and numerical results for Young modulus are justified by the nature of the model, which is intrinsically stiffer [49]. Moreover, LPBFed structures may present internal defects, which are not simulated and can increase the mismatch in the results between FEM and EXP [16]. On the contrary, simulations perfectly predict the first peak force values for each sample: the average discrepancy between average experimental and numerical results is about 1 %, which confirms the reliability of the model for the

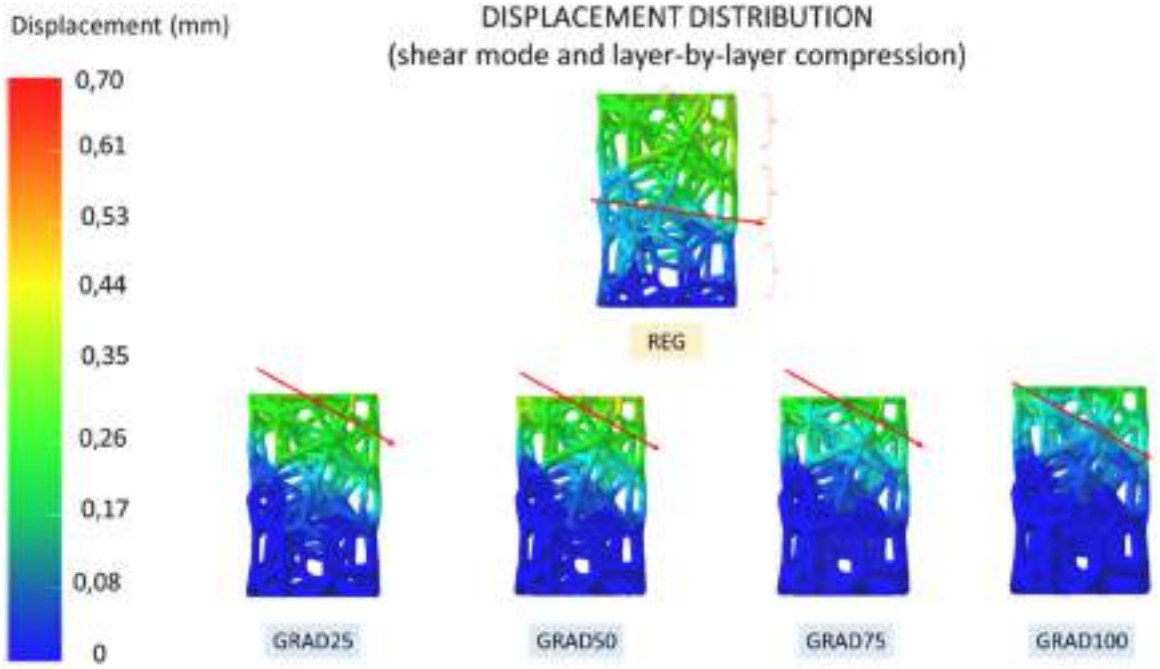

Fig. 13. Numerical results: displacement map. The brackets in REG ULSs indicate the layer-by-layer displacement which lead to a layer-by-layer failure. The FGLSs exhibit a more shear mode displacement.

mechanical evaluation of stress and displacement distribution of the samples before first failure.

Deformation takes place in shear mode in all the studied geometries, as demonstrated by the displacement maps reported in Fig. 13 and observed in the video frame images (Fig. 10).

The Von Mises stress distribution is highlighted in Fig. 14(a-c-e-g-i). While for REG ULS model the stress is evenly distributed along the entire model, for FGLSs the stress is concentrated in the upper part: similar finding has been obtained by the observation of experimental tests (Fig. 9). The evaluation of yielding regions at first peak force (Fig. 14b-d-f-h-l) is consistent with the Von Mises stress distribution and with the experimental observations. Indeed, while the REG ULS exhibits a uniform yielding along the entire sample, FGLSs present an evident concentration of yielded areas in the volume characterized by thinner struts.

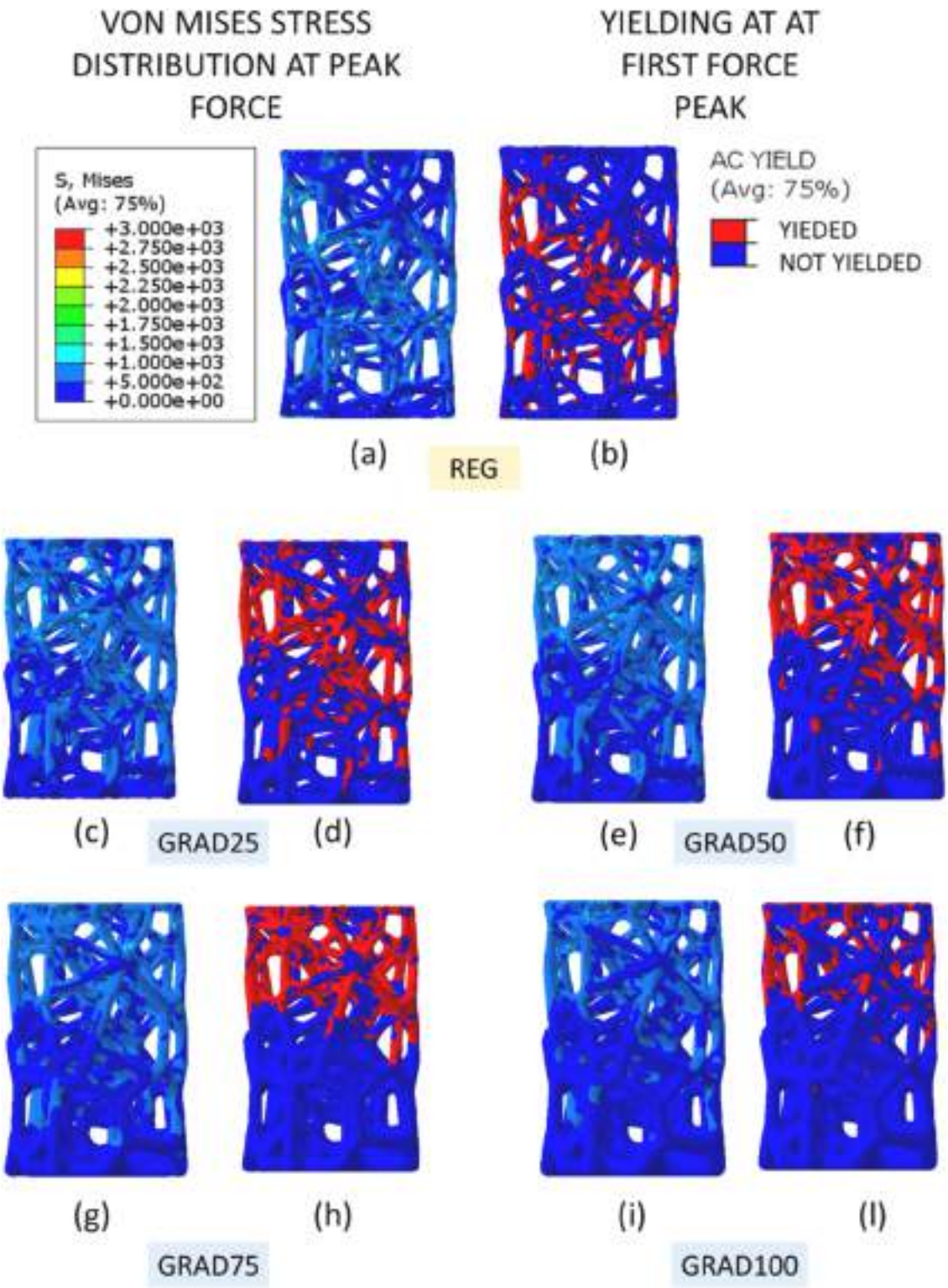

Fig. 14. Von Mises stress distribution at peak force for each samples (a-c-e-g-i); yielding map at peak force for each sample (b-d-f-h-l).

4. Conclusions

In this work, FGLSs based on Voronoi tessellation are designed, produced by LPBF, qualitatively assessed and mechanically evaluated, by means of both numerical and experimental investigations in order to evaluate their performance, feasibility and the impact of both relative densities which changes among the samples and the thickness gradient. For a better evaluation of the thickness gradient, a comparison with a constant thickness Voronoi lattice structure (REG05 ULSs) with the same architectural arrangement of struts is performed. The following conclusions stem from this work:

- The designed structures are successfully realized by means of LPBF technology in Ti6Al4Vpowder. The dimensional deviation is about 0.09 mm, which is compatible with the literature optimum;
- The low standard deviation in the experimental compression tests confirms good reproducibility of the LPBF process for the realization of similar complex lattice structures;
- Constant-thickness structures (REG05 ULSs) exhibit a constant energy absorption upon the whole deformation range, while FGLSs show a progressively increasing efficiency in absorbing energy at increasing strain. Moreover, the grater is the thickness gradient, the greater is the improvement in energy absorption, especially for region 2 (5–15 % of strain) and region 3 (15–25 % of strain);
- Strong linear correlation between relative young modulus and relative density is observed regardless the thickness gradient.
- In Voronoi lattice based structures, the struts' stochastic arrangement results mainly in bending failure, more evident for graded-structures and less evident for constant thickness structures;
- The numerical analysis confirms the stress and strain distribution hypothesized from the experimental tests, make the simulation reliable and spendable for further analysis.

These findings contribute to the broader understanding of Voronoi-based ULSs and FGLSs, which can be applied in various engineering fields.

CRediT authorship contribution statement

Chiara Bregoli: Writing – review & editing, Writing – original draft, Visualization, Software, Methodology, Investigation, Formal analysis, Data curation, Conceptualization. **Jacopo Fiocchi:** Writing – review & editing, Writing – original draft, Methodology, Investigation, Formal analysis, Data curation, Conceptualization. **Mehrshad Mehrpouya:** Writing – review & editing, Methodology, Investigation, Formal analysis. **Laura Maria Vergani:** Writing – review & editing, Supervision, Project administration, Methodology, Formal analysis. **Ausonio Tuissi:** Writing – review & editing, Supervision, Project administration. **Carlo Alberto Biffi:** Writing – review & editing, Supervision, Project administration, Conceptualization.

Declaration of competing interest

The authors declare that they have no known competing financial interests or personal relationships that could have appeared to influence the work reported in this paper.

Acknowledgements

The authors would like to thank Nicola Bennato and Enrico Bassani from CNR ICMATE for their assistance in the experiments. Also, special thanks to Eslam Salaheldin Abdelhady from UTwente for his support in the micro-CT experiment.

References

[1] Y. Mu, Y. Jin, H. Ji, W. Wang, S. Zou, C. Zhang, J. Du, Mechanical properties of a novel hierarchical cellular structure architectured with minimal surfaces and Voronoi-tessellation, Compos. Struct. 325 (2023) 117610, https://doi.org/10.1016/j.compstruct.2023.117610.
[2] S. Dadbakhsh, M. Speirs, J.P. Kruth, J. Van Humbeeck, Influence of SLM on shape memory and compression behaviour of NiTi scaffolds, CIRP Ann. - Manuf. Technol. 64 (2015) 209–212, https://doi.org/10.1016/j.cirp.2015.04.039.
[3] S. Chowdhury, N. Yadaiah, C. Prakash, S. Ramakrishna, S. Dixit, L.R. Gupta, D. Buddhi, Laser powder bed fusion: a state-of-the-art review of the technology, materials, properties & defects, and numerical modelling, J. Mater. Res. Technol. 20 (2022) 2109–2172, https://doi.org/10.1016/j.jmrt.2022.07.121.
[4] Z. Yu, R. Xin, Z. Xu, L. Sha, L. Chen, Y. Zhu, P. Liang, Z. Zhang, Z. Liu, Q. Cao, Shock-resistant and energy-absorbing properties of bionic NiTi lattice structure manufactured by SLM, J. Bionic Eng. 19 (2022) 1684–1698, https://doi.org/10.1007/s42235-022-00221-0.
[5] F. Bartolomeu, M.M. Costa, N. Alves, G. Miranda, F.S. Silva, Additive manufacturing of NiTi-Ti6Al4V multi-material cellular structures targeting orthopedic implants, Opt. Lasers Eng. 134 (2020) 106208, https://doi.org/10.1016/j.optlaseng.2020.106208.
[6] A. du Plessis, N. Razavi, M. Benedetti, S. Murchio, M. Leary, M. Watson, D. Bhate, F. Berto, Properties and applications of additively manufactured metallic cellular materials: a review, Prog. Mater. Sci. 125 (2022) 100918, https://doi.org/10.1016/j.pmatsci.2021.100918.
[7] L. Bai, Y. Xu, X. Chen, L. Xin, J. Zhang, K. Li, Y. Sun, Improved mechanical properties and energy absorption of Ti6Al4V laser powder bed fusion lattice structures using curving lattice struts, Mater. Des. 211 (2021) 110140, https://doi.org/10.1016/j.matdes.2021.110140.
[8] B. Herath, S. Suresh, D. Downing, S. Cometta, R. Tino, N.J. Castro, M. Leary, B. Schmutz, M.L. Wille, D.W. Hutmacher, Mechanical and geometrical study of 3D printed Voronoi scaffold design for large bone defects, Mater. Des. 212 (2021) 110224, https://doi.org/10.1016/j.matdes.2021.110224.
[9] M. Fantini, M. Curto, F. De Crescenzio, A method to design biomimetic scaffolds for bone tissue engineering based on Voronoi lattices, Virtual Phys. Prototyp. 11 (2016) 77–90, https://doi.org/10.1080/17452759.2016.1172301.
[10] M. Fantini, M. Curto, Interactive design and manufacturing of a Voronoi-based biomimetic bone scaffold for morphological characterization, Int. J. Interact. Des. Manuf. 12 (2018) 585–596, https://doi.org/10.1007/s12008-017-0416-x.
[11] Y. Du, H. Liang, D. Xie, N. Mao, J. Zhao, Z. Tian, C. Wang, L. Shen, Design and statistical analysis of irregular porous scaffolds for orthopedic reconstruction based on Voronoi tessellation and fabricated via selective laser melting (SLM), Mater. Chem. Phys. 239 (2020) 1–9, https://doi.org/10.1016/j.matchemphys.2019.121968.
[12] F. Caiazzo, V. Alfieri, S.L. Campanelli, V. Errico, Additive manufacturing and mechanical testing of functionally-graded steel strut-based lattice structures, J. Manuf. Process. 83 (2022) 717–728, https://doi.org/10.1016/j.jmapro.2022.09.031.
[13] X. Wang, S. Xu, S. Zhou, W. Xu, M. Leary, P. Choong, M. Qian, M. Brandt, Y.M. Xie, Topological design and additive manufacturing of porous metals for bone scaffolds and orthopaedic implants: a review, Biomaterials 83 (2016) 127–141, https://doi.org/10.1016/j.biomaterials.2016.01.012.
[14] E. Marin, A. Lanzutti, Biomedical applications of titanium alloys: a comprehensive review, Materials (Basel) 17 (2024), https://doi.org/10.3390/ma17010114.
[15] X. Cheng, K. Wei, R. He, Y. Pei, D. Fang, The equivalent thermal conductivity of lattice core sandwich structure: a predictive model, Appl. Therm. Eng. 93 (2016) 236–243, https://doi.org/10.1016/j.applthermaleng.2015.10.002.
[16] S. Dhiman, M. Singh, S.S. Sidhu, M. Bahraminasab, D.Y. Pimenov, T. Mikolajczyk, Cubic lattice structures of Ti6Al4V under compressive loading: towards assessing the performance for hard tissue implants alternative, Materials (Basel) 14 (2021), https://doi.org/10.3390/ma14143866.
[17] S. Pramanik, K.P. Hoyer, M. Schaper, Experimental and finite element method investigation on the compression behaviour of FCCZ and BCC lattice structures of additively manufactured Fe-3Si samples, Rapid Prototyp. J. 29 (2023) 1257–1269, https://doi.org/10.1108/RPJ-06-2022-0190.
[18] C. Pan, Y. Han, J. Lu, Design and optimization of lattice structures: a review, Appl. Sci. 10 (2020) 6374, https://doi.org/10.3390/app10186374.
[19] Z. Dong, X. Zhao, Application of TPMS structure in bone regeneration, Eng. Regen. 2 (2021) 154–162, https://doi.org/10.1016/j.engreg.2021.09.004.
[20] C. Yan, L. Hao, A. Hussein, P. Young, Ti-6Al-4V triply periodic minimal surface structures for bone implants fabricated via selective laser melting, J. Mech. Behav. Biomed. Mater. 51 (2015) 61–73, https://doi.org/10.1016/j.jmbbm.2015.06.024.
[21] G. Wang, L. Shen, J. Zhao, H. Liang, D. Xie, Z. Tian, C. Wang, Design and compressive behavior of controllable irregular porous scaffolds: based on Voronoi-tessellation and for additive manufacturing, ACS Biomater. Sci. Eng. 4 (2018) 719–727, https://doi.org/10.1021/acsbiomaterials.7b00916.
[22] D. Almonti, G. Baiocco, V. Tagliaferri, N. Ucciardello, Design and mechanical characterization of Voronoi structures manufactured by indirect additive manufacturing, Materials (Basel) 13 (2020) 1–12, https://doi.org/10.3390/ma13051085.
[23] X. An, P.L. Chong, I. Zohourkari, S. Roy, A. Merdji, C. Linda Gnanasagaran, F. Faraji, L.K. Moey, M.H. Yazdi, Mechanical influence of tissue scaffolding design with different geometries using finite element study, Proc. Inst. Mech. Eng. Part H J. Eng. Med. 237 (2023) 1008–1016, https://doi.org/10.1177/09544119231187685.

[24] A. Okabe, Spatial tessellations, Int. Encycl. Geogr. (2017) 1–11, https://doi.org/10.1002/9781118786352.wbieg0601.
[25] M. Araya, M. Jaskari, T. Rautio, T. Guillén, A. Järvenpää, Assessing the compressive and tensile properties of TPMS-Gyroid and stochastic Ti64 lattice structures: a study on laser powder bed fusion manufacturing for biomedical implants, J. Sci. Adv. Mater. Devices 9 (2024) 100663, https://doi.org/10.1016/j.jsamd.2023.100663.
[26] Y. Xiong, Z. Han, J. Qin, L. Dong, H. Zhang, Y. Wang, H. Chen, X. Li, Effects of porosity gradient pattern on mechanical performance of additive manufactured Ti-6Al-4V functionally graded porous structure, Mater. Des. 208 (2021) 109911, https://doi.org/10.1016/j.matdes.2021.109911.
[27] B. Jagadeesh, M. Duraiselvam, K.G. Prashanth, Deformation behavior of metallic lattice structures with symmetrical gradients of porosity manufactured by metal additive manufacturing, Vacuum. 211 (2023) 111955, https://doi.org/10.1016/j.vacuum.2023.111955.
[28] A. Seharing, A.H. Azman, S. Abdullah, A review on integration of lightweight gradient lattice structures in additive manufacturing parts, Adv. Mech. Eng. 12 (2020) 1–21, https://doi.org/10.1177/1687814020916951.
[29] Y. Lin, W. Shi, J. Li, Y. Liu, S. Liu, J. Li, Evaluation of mechanical properties of Ti–6Al–4V BCC lattice structure with different density gradient variations prepared by L-PBF, Mater. Sci. Eng. A. 872 (2023), https://doi.org/10.1016/j.msea.2023.144986.
[30] Y. Li, Z. Feng, L. Hao, L. Huang, C. Xin, Y. Wang, E. Bilotti, K. Essa, H. Zhang, Z. Li, F. Yan, T. Peijs, A review on functionally graded materials and structures via additive manufacturing: from multi-scale design to versatile functional properties, Adv. Mater. Technol. 5 (2020), https://doi.org/10.1002/admt.201900981.
[31] Y. Lin, W. Shi, J. Li, Y. Liu, S. Liu, J. Li, Evaluation of mechanical properties of Ti–6Al–4V BCC lattice structure with different density gradient variations prepared by L-PBF, Mater. Sci. Eng. A 872 (2023) 144986, https://doi.org/10.1016/j.msea.2023.144986.
[32] W. Pokojski, P. Pokojska, Voronoi diagrams—inventor, method, applications, Polish Cartogr. Rev. 50 (2018) 141–150, https://doi.org/10.2478/pcr-2018-0009.
[33] M. Park, M.P. Venter, A. Du Plessis, A lattice structure coupon sample for build quality control in metal additive manufacturing, Mater. Des. 235 (2023) 112436, https://doi.org/10.1016/j.matdes.2023.112436.
[34] H.Y. Lei, J.R. Li, Z.J. Xu, Q.H. Wang, Parametric design of Voronoi-based lattice porous structures, Mater. Des. 191 (2020) 108607, https://doi.org/10.1016/j.matdes.2020.108607.
[35] C. Bregoli, C.A. Biffi, A. Tuissi, F. Buccino, Effect of trabecular architectures on the mechanical response in osteoporotic and healthy human bone, Med. Biol. Eng. Comput. (2024), https://doi.org/10.1007/s11517-024-03134-8.
[36] R. Domander, A.A. Felder, M. Doube, BoneJ2 - refactoring established research software, (2021) 1–13. https://doi.org/10.12688/wellcomeopenres.16619.2.
[37] M.F. Ashby, The properties of foams and lattices, Philos. Trans. R. Soc. A Math. Phys. Eng. Sci. 364 (2006) 15–30, https://doi.org/10.1098/rsta.2005.1678.
[38] C. Bregoli, J. Fiocchi, C.A. Biffi, A. Tuissi, Additively manufactured medical bone screws: an initial study to investigate the impact of lattice-based Voronoi structure on implant primary stability, Rapid Prototyp. J. 30 (2024) 60–72, https://doi.org/10.1108/RPJ-10-2022-0363.
[39] W. Chen, D. Gu, J. Yang, Q. Yang, J. Chen, X. Shen, Compressive mechanical properties and shape memory effect of NiTi gradient lattice structures fabricated by laser powder bed fusion, Int. J. Extrem. Manuf. 4 (2022), https://doi.org/10.1088/2631-7990/ac8ef3.
[40] M.F. Gibson, L.J. Ashby, Cellular Solids: Structure and Properties, second ed., Cambridge University Press, 1997.
[41] S. Lu, M. Zhang, S. Guo, B. Hur, X. Yue, Numerical investigation of impact behavior of strut-based cellular structures designed by spatial Voronoi tessellation, Metals (Basel) 12 (2022), https://doi.org/10.3390/met12071189.
[42] S.J. Hollister, N. Kikuchi, Homogenization theory and digital imaging: a basis for studying the mechanics and design principles of bone tissue, Biotechnol. Bioeng. 43 (1994) 586–596, https://doi.org/10.1002/bit.260430708.
[43] Q. Luo, L. Yin, T.W. Simpson, A.M. Beese, Effect of processing parameters on pore structures, grain features, and mechanical properties in Ti-6Al-4V by laser powder bed fusion, Addit. Manuf. 56 (2022) 102915, https://doi.org/10.1016/j.addma.2022.102915.
[44] T. Maconachie, M. Leary, B. Lozanovski, X. Zhang, M. Qian, O. Faruque, M. Brandt, SLM lattice structures: properties, performance, applications and challenges, Mater. Des. 183 (2019), https://doi.org/10.1016/j.matdes.2019.108137.
[45] M. Speirs, B. Van Hooreweder, J. Van Humbeeck, J.P. Kruth, Fatigue behaviour of NiTi shape memory alloy scaffolds produced by SLM, a unit cell design comparison, J. Mech. Behav. Biomed. Mater. 70 (2017) 53–59, https://doi.org/10.1016/j.jmbbm.2017.01.016.
[46] W. Chen, Q. Yang, S. Huang, J.J. Kruzic, X. Li, Compression behavior of graded NiTi Gyroid-structures fabricated by laser powder bed fusion additive manufacturing under monotonic and cyclic loading, JOM 73 (2021) 4154–4165, https://doi.org/10.1007/s11837-021-04938-x.
[47] H. Yin, W. Zhang, L. Zhu, F. Meng, J. Liu, G. Wen, Review on lattice structures for energy absorption properties, Compos. Struct. 304 (2023) 116397, https://doi.org/10.1016/j.compstruct.2022.116397.
[48] T. Maconachie, M. Leary, B. Lozanovski, X. Zhang, M. Qian, O. Faruque, M. Brandt, SLM lattice structures: properties, performance, applications and challenges, Mater. Des. 183 (2019) 108137, https://doi.org/10.1016/j.matdes.2019.108137.
[49] I.A. Ashcroft, Handbook of Adhesion Technology, 2011, https://doi.org/10.1007/978-3-642-01169-6.